Full-vectorial analysis of high-index-contrast coupled channel waveguides

Md. Zahed M. Khan* and Husain Ali Jamid

King Fahd University of Petroleum and Minerals, Dhahran 31261, Saudi Arabia

*Corresponding author: zahedmk@yahoo.co.in

Received 9 March 2009; revised 15 June 2009; accepted 28 June 2009;
posted 14 July 2009 (Doc. ID 108421); published 27 July 2009

Coupling of two identical channel waveguides separated by an air gap is analyzed. The coupled structure exhibits a strong refractive index contrast in both the transverse and longitudinal dimensions, which necessitates the use of a full-vectorial model. The 3D full-vectorial bidirectional method-of-lines beam propagation is utilized for this purpose. The effect of the transverse and longitudinal displacements on the modal reflectivity and modal transmissivity of the fundamental TE-like and TM-like modes is reported. Numerical results are presented for both the full-vectorial model and the approximate semivectorial model. A significant difference between the predictions of these two models is seen. © 2009 Optical Society of America

OCIS codes: 130.2790, 230.7380, 130.0130.

1. Introduction

Guided wave structures are essential elements in optical communications for the purpose of filtering, coupling, switching, modulating, power splitting, etc. They have been investigated widely in 2D workspaces utilizing various numerical techniques and in both low-high-index-contrast material systems [1–7]. However, it is well known that high-index-contrast structures cannot be well approximated by using 2D models and thus require a rigorous 3D workspace for analysis. The advent of fast processors and large memory storage capabilities has initiated the development and improvement of various numerical techniques to model different waveguide problems in a 3D workspace rather than the 2D environment. This includes the waveguide facets and step discontinuities utilizing the finite difference time domain method [8], radiation modes method [9], transfer matrix method [10], a field-based method [11], finite element method [12] and bidirectional method-of-lines beam propagation method (MoL-BPM) [13]. Moreover, multidiscontinuity problems, for instance, coupled waveguides, tapered waveguides, and polarization rotators, have been addressed by employing the free space radiation mode method [14], mode matching method, [15] and method of lines [16]. However, these reported waveguide problems are based in general on low-index-contrast material system under the 3D semivectorial approximation. Improved 3D numerical techniques that are based on the transverse magnetic formulation and the full-vectorial nature of the field rather than semivectorial approximation have recently been reported [17,18]. These MoL-BPM techniques account rigorously for the longitudinal boundary condition and are, in general, numerically efficient. With these promising features, they can be applied to both low-and high-index-contrast waveguide problems. They have been applied to high-index-contrast waveguide facets [17], coupled waveguides, and polarization rotators [18] to show the effectiveness of the techniques rather than investigating them, in general.

In this work, we propose to analyze the high-index-contrast coupled channel waveguides utilized in [18]. The arrangement consists of two aligned raised channel waveguides separated by an air gap forming two strong longitudinal discontinuities. The structure may represent the practical problem of determining the transmission from a laser, across an air

---

0003-6935/09/224468-07$15.00/0

gap, and into a waveguide. The influence of the transverse separation (vertical and lateral) on the modal reflectivity and modal transmissivity of the coupled waveguides will be presented, which closely simulates a misaligned laser with a waveguide. To the best of our knowledge, such an investigation has not been reported in the literature. Numerical results of the fundamental TE-like and TM-like modes utilizing the 3D full-vectorial MoL-BPM numerical technique [18] will be reported. Moreover, the results obtained from both the full-vectorial and the semivectorial formulations will be shown for comparison and to highlight the difference between the predictions of both formulations.

2. Background

A brief outline of the numerical approach that is based on the transverse magnetic field formulation is presented. The reader is referred to [17,18] for details. Consider the 3D wave equation that upon discretization in the transverse dimensions x and y, using p and q sample points, respectively, yields the following equation [17]:

$$\frac{\mathrm{d}^2}{\mathrm{d}z^2}\bar{\mathbf{H}} + \hat{\mathbf{C}}^2\bar{\mathbf{H}} = \bar{\mathbf{0}}. \tag{1}$$

The general solution of the above equation is $\bar{\mathbf{H}} = e^{j\hat{\mathbf{C}}z}\bar{\mathbf{A}} + e^{-j\hat{\mathbf{C}}z}\bar{\mathbf{B}}$. $\bar{\mathbf{H}} = (\bar{\mathbf{H}}_\mathbf{x}\,\bar{\mathbf{H}}_\mathbf{y})^T$, where the column vectors $\bar{\mathbf{H}}_\mathbf{x}$ and $\bar{\mathbf{H}}_\mathbf{y}$ contain the magnetic field component H_x and H_y in discrete form, respectively. The square matrix $\hat{\mathbf{C}}^2$ is the characteristic matrix that accounts for the spatial derivatives in the x–y plane as well as the coupling between the transverse magnetic field components H_x and H_y [17]. The square matrices $e^{\pm j\hat{\mathbf{C}}z}$ account for the forward and the backward fields, respectively. The transverse electric field components, in discrete form, can be obtained from the transverse magnetic field components by using the following equation [18]:

$$\bar{\mathbf{E}} = \hat{\mathbf{S}}\bar{\mathbf{H}}, \tag{2}$$

where $\bar{\mathbf{E}} = (\bar{\mathbf{E}}_\mathbf{y}\ -\bar{\mathbf{E}}_\mathbf{x})^T$ and where $\bar{\mathbf{E}}_\mathbf{x}$ and $\bar{\mathbf{E}}_\mathbf{y}$ contain the discretized values of the transverse electric field components E_x and E_y, respectively. The square matrix $\hat{\mathbf{S}} = \left(jk_0^{-1}\sqrt{\mu_0\varepsilon_0^{-1}}\right)\hat{\mathbf{N}}^{-2}(\hat{\mathbf{O}} - \hat{\mathbf{C}}^2)(j\hat{\mathbf{C}})^{-1}$, where $\hat{\mathbf{N}}^2$ contains the square of the refractive index distribution and $\hat{\mathbf{O}}$ accounts for the transverse differential operators in discretized form. The square matrix $(j\hat{\mathbf{C}})^{-1}$ corresponds to the integration operator that appears in the transverse electric field relation. It is noteworthy that the size of the square matrix $\hat{\mathbf{S}}$ will be $pq \times pq$ for the semivectorial formulation and $2pq \times 2pq$ for the full-vectorial model.

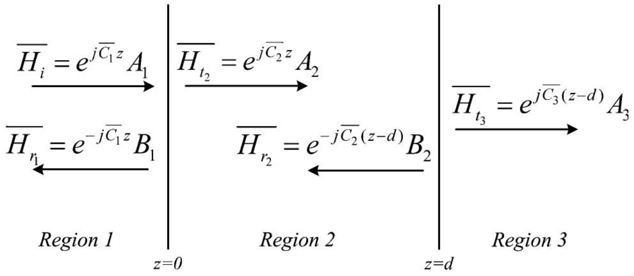

Fig. 1. Two abrupt longitudinal discontinuities placed at $z = 0$ and $z = d$.

Now, consider two abrupt longitudinal discontinuities placed at $z = 0$ and $z = d$, shown in Fig. 1, with the input transverse magnetic field assumed to be incident from the left at $z = 0$. The transmitted and the reflected magnetic fields of the structure shown in Fig. 1 can be obtained by applying the continuity of the transverse magnetic and electric fields at these longitudinal boundaries ($z = 0$ and $z = d$). This results in a set of four equations that can be cast into a simple linear matrix relation as shown [18]:

$$\hat{\mathbf{\Gamma}}\bar{\mathbf{X}} = \bar{\Lambda}, \tag{3}$$

where

$$\hat{\mathbf{\Gamma}} = \begin{bmatrix} (\hat{\mathbf{S}}_1 + \hat{\mathbf{S}}_2) & -2\hat{\mathbf{S}}_2\hat{\mathbf{P}}_2 & \hat{\mathbf{0}} & \hat{\mathbf{0}} \\ \hat{\mathbf{0}} & (\hat{\mathbf{S}}_2 + \hat{\mathbf{S}}_3) & (\hat{\mathbf{S}}_3 - \hat{\mathbf{S}}_2)\hat{\mathbf{P}}_2 & \hat{\mathbf{0}} \\ \hat{\mathbf{0}} & (\hat{\mathbf{S}}_1 - \hat{\mathbf{S}}_2)\hat{\mathbf{P}}_2 & (\hat{\mathbf{S}}_1 + \hat{\mathbf{S}}_2) & \hat{\mathbf{0}} \\ \hat{\mathbf{0}} & \hat{\mathbf{0}} & -2\hat{\mathbf{S}}_2\hat{\mathbf{P}}_2 & (\hat{\mathbf{S}}_2 + \hat{\mathbf{S}}_3) \end{bmatrix}$$

$$\bar{\Lambda} = \begin{bmatrix} (\hat{\mathbf{S}}_1 - \hat{\mathbf{S}}_2)\bar{\mathbf{A}}_1 \\ \bar{\mathbf{0}} \\ 2\hat{\mathbf{S}}_1\bar{\mathbf{A}}_1 \\ \bar{\mathbf{0}} \end{bmatrix}.$$

The column vector $\bar{\mathbf{X}} = [\bar{\mathbf{B}}_1{}^{-}\mathbf{B}_2{}^{-}\mathbf{A}_2{}^{-}\mathbf{A}_3]^T$ contains the required reflected ($\bar{\mathbf{B}}_1$) and transmitted ($\bar{\mathbf{A}}_3$) magnetic fields in addition to the fields within the discontinuous structure. The term $\bar{\mathbf{A}}_1$ appearing in the known column vector $\bar{\Lambda}$ represents the incident magnetic field, while the square matrix $\hat{\mathbf{P}}_2 = e^{j\hat{\mathbf{C}}_2 d}$ is the propagation matrix. The square matrix $\hat{\mathbf{C}}$, which is required for obtaining the matrix $\hat{\mathbf{S}}$, has been obtained by using Padé approximants of the square root operator, and the matrix $\hat{\mathbf{P}}$ has been obtained by using Padé approximants of the exponential operator [7,18]. Equation (3) is a simple matrix relation that can be solved iteratively utilizing the biconjugate stabilized algorithm (BI-CGSTAB)[19]. However, solving Eq. (3) directly degrades the performance of BI-CGSTAB, leading to an unacceptably large number of iterations or even failure to achieve convergence. To overcome this difficulty, Eq. (3) is preconditioned in a manner similar to the one reported in [18], before application of BI-CGSTAB.

3. Numerical Results

In this section, the numerical approach is first demonstrated for accuracy and later applied to analyze the coupled channel waveguides utilized in [18]. The results of both the semivectorial and full-vectorial models are shown for comparison, assuming the fundamental TE-like (TE_{00}) and TM-like (TM_{00}) modes to be incident on the first longitudinal discontinuity placed at $z = 0$. The Padé orders associated with the square root and the propagation operators are fixed at 4 and 8, respectively [18]. In addition, the waveguides are surrounded by a perfectly matched absorbing layer from all sides to absorb the radiative field [20].

Since the analysis requires calculating the fundamental TE-like and TM-like mode transmissivity (the ratio of the transmitted mode power to the incident mode power) and mode reflectivity (the ratio of the reflected mode power to the incident mode power), the procedure used for calculating these values will be briefly explained. The modal transmissivity $T_{m'm}$, associated with the transmitted mode m' and the incident mode m, is given by

$$T_{m'm} = P^t_{m'}/P^i_m, \tag{4}$$

where the incident mode power P^i_m and the transmitted mode power $P^t_{m'}$, respectively, are given by

$$P^i_m = 0.5 \iint \mathrm{Re}(E^i_{x,m}H^{i*}_{y,m} - E^i_{y,m}H^{i*}_{x,m})\mathrm{d}x\mathrm{d}y, \tag{5}$$

$$P^t_{m'} = 0.5 \iint \mathrm{Re}(E^t_{x,m'}H^{t*}_{y,m'} - E^t_{y,m'}H^{t*}_{x,m'})\mathrm{d}x\mathrm{d}y. \tag{6}$$

The superscripts i and t refer to the incident and transmitted fields, respectively, and the asterisk indicates the complex conjugate. The transverse electric and magnetic field components appearing in Eqs. (5) and (6) are modal field components, as indicated by the subscripts m and m'. The modal field associated with the incident mode m is readily available, because the incident field is purely modal. However, the transmitted modal field needs to be extracted from the transmitted field before application of Eq. (6). This can be done by first finding the associated transmitted mode amplitude $\alpha^t_{m'}$ and then multiplying it by a suitably normalized version of the transmitted modal field. A simple numerical procedure that can be used to calculate the mode amplitudes has been reported in [16]. This method may also be used to calculate the modal reflectivity $R_{m'm}$ associated with the reflected mode m' and the incident mode m.

Now, consider the coupled buried waveguide structure shown in Fig. 2(a). It consists of two identical buried low-index-contrast waveguides separated by an air gap of width L. All the relevant waveguide parameters are shown in the figure. The arrangement has been previously reported under the 3D semivectorial approximation [14,15]. Figure 3 shows the variation of the modal transmissivity of the TE-like and TM-like modes of the coupled waveguides as a function of the air gap width L, based on the semivectorial model. The results reported in [14] and our results are observed to be virtually indistinguishable. This establishes the accuracy of the present technique. However, it is observed that the low-index-contrast material system of the selected structure does not show any difference between the semivectorial and the full-vectorial representations of the field.

To further ascertain the accuracy of the numerical approach under the high-index-contrast environment, another coupled channel waveguide shown in Fig. 2(b) is considered [18]. The structure consists of two identical channel waveguides separated by an air gap of width L. The arrangement exhibits strong discontinuities in both the longitudinal and the transverse dimensions. All the relevant waveguide parameters are indicated in the same figure, and the air gap width is fixed at $L = 0.1\,\mu$m. In this case, the waveguide parameters are unaltered except for the waveguide core width w_x, which is varied from 1.0 to 5.0 μm. The calculated result of the fundamental TE-like and TM-like mode reflectivity and transmissivity as a function of the core width w_x is shown in Fig. 4. The results of both the semivectorial and the full-vectorial models are shown in the figure. Notice that when the waveguide core width w_x increases, the modal transmissivity and reflectivity values obtained by using the semivectorial and full-vectorial models approach each other. They subsequently approach the calculated results of the corresponding 2D model, as indicated by the arrows shown in the figure. The results shown in Fig. 4 further ascertain the accuracy of the technique. It is noteworthy to mention that when the waveguide width w_x becomes small, the results obtained from both the semivectorial and full-vectorial models show a substantial difference in the modal transmissivity values [see Fig. 4(b)]. The deviation in the results of the semivectorial and full-vectorial models is clearly due to the full-vectorial model's accounting for the minor field as well. However, the modal reflectivity values as predicted by both models remain generally in good agreement for the entire range of the waveguide core width w_x [see Fig. 4(a)].

The numerical approach demonstrated above will now be utilized to analyze the coupled high-index-contrast channel waveguides shown in Fig. 2(b). We will first consider the effect of the air gap width L on the fundamental TE-like and TM-like mode responses. As mentioned earlier, this arrangement may simulate power coupling from a laser, through air, and into the optical waveguide. The waveguide core width is fixed at $w_x = 1.0\,\mu$m, keeping all the remaining parameters of the structure unaltered. The full-vectorial transverse magnetic field patterns of the fundamental TE-like and TM-like modes of the input waveguide are shown in Fig. 5. The corresponding calculated mode effective indices are 3.45647 and 3.46508, respectively. Figures 6 and 7, respectively, show the calculated fundamental TE-like and TM-like mode responses as a function of the air gap width L. These two figures show the

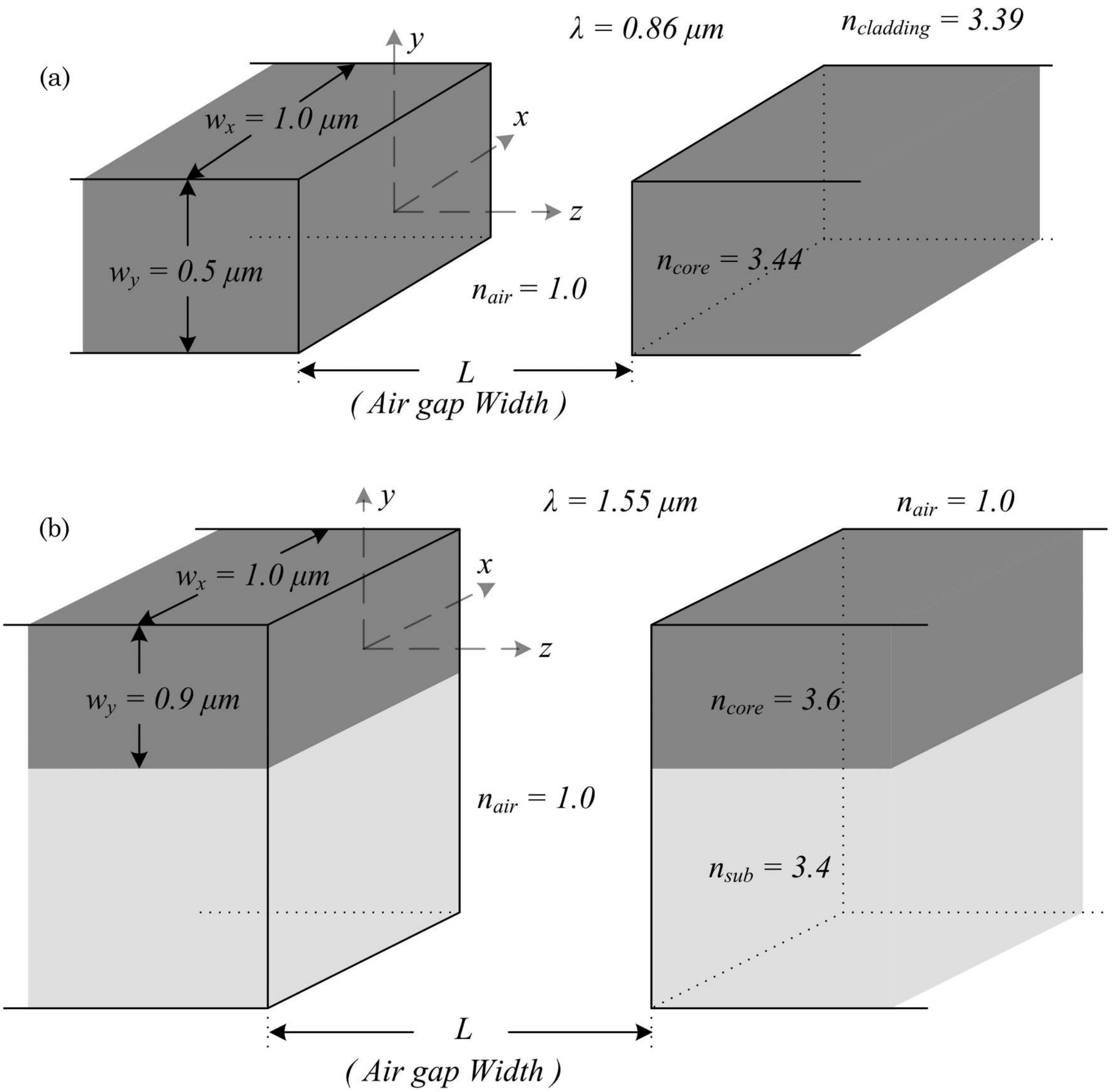

Fig. 2. (a) Two identical coupled buried waveguides and (b) two identical coupled raised channel waveguides.

calculated mode reflectivity, transmissivity, and fraction of radiated power (FPR) under the semivectorial and full-vectorial assumptions. Since the channel waveguides depicted in Fig. 2(b) are single mode, the FPR may be calculated by using the relationship FPR = 1 – modal reflectivity – modal transmissivity, by assuming negligible polarization cross coupling. Again, a substantial difference in the calculated results obtained from the semivectorial and the full-vectorial models are noticeable for the entire range of the air gap width under consideration. As shown in Figs. 6 and 7, the modal reflectivities associated with the TE-like and TM-like fundamental modes, respectively, attain their maximum values for an air gap width $L \approx 0.5\,\mu$m, which is due to constructive interference (Fabry–Perot cavity effect). Throughout this work the maximum longitudinal step size is set to $\Delta z = 0.1\,\mu$m. In addition, convergent results typically require a transverse mesh density of 20 mesh points per micrometer. The BI-CGSTAB routine requires about 15 to 20 iterations to converge.

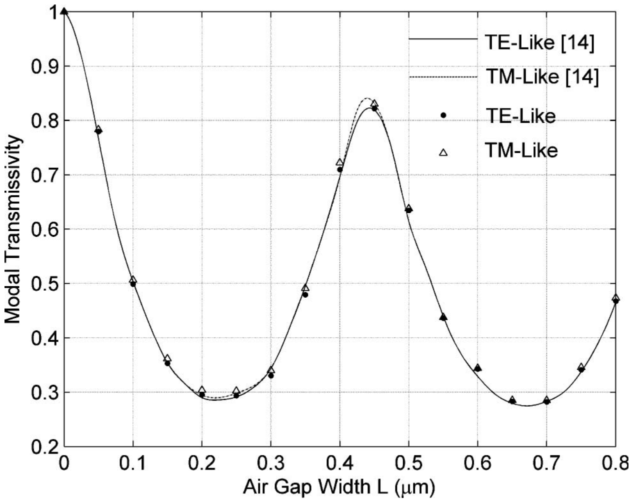

Fig. 3. Calculated semivectorial results of the fundamental TE-like and TM-like mode transmissivity corresponding to the coupled waveguides shown in Fig. 2(a) at the operating wavelength $\lambda = 0.86\,\mu$m.

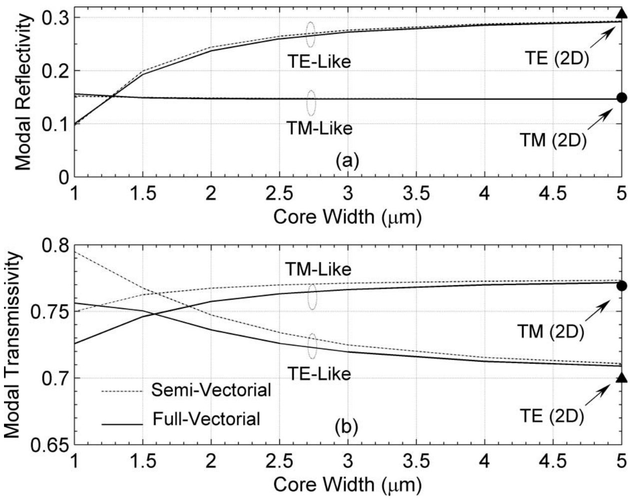

Fig. 4. Fundamental TE-like and TM-like (a) mode reflectivity and (b) mode transmissivity, corresponding to the coupled channel waveguides shown in Fig. 2(b) at the operating wavelength $\lambda = 1.55\,\mu$m and a fixed air gap width $L = 0.1\,\mu$m.

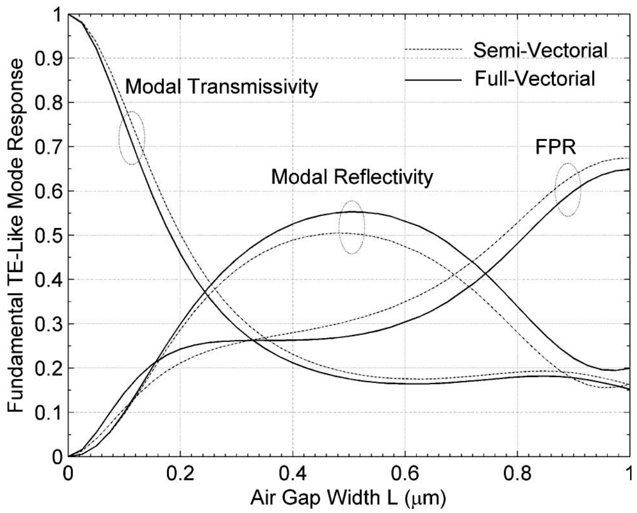

Fig. 6. Fundamental TE-like mode response corresponding to the coupled channel waveguides shown in Fig. 2(b).

Further to the investigation of the coupled channel waveguides, if the right channel waveguide (output waveguide) of Fig. 2(b) is displaced from its original position in the transverse direction (horizontal or vertical), the power coupled to the output waveguide is expected to decrease with an increase in the modal reflectivity and FPR. This may again emulates the practical problem of a misaligned laser with an optical waveguide. In order to examine this assumption, the vertical axis (y axis) of the output waveguide is moved in the horizontal direction (along the x axis) with respect to the vertical axis of the input waveguide. This displacement is termed the horizontal displacement Δx throughout this paper. With this arrangement, the mode reflectivity and transmissivity of the coupled channel waveguides [see Fig. 2(b)] is calculated as a function of the horizontal displacement Δx. The analysis is carried out under two situations. The first situation considered is when the input and the output waveguides have no longitudinal separation (i.e., $L = 0\,\mu$m). In the second situation, the longitudinal separation between the two channel waveguides is fixed at $L = 0.1\,\mu$m, resulting in a small air gap. The remaining parameters of the waveguides are kept unchanged. The calculated results are shown in Figs. 8 and 9 which correspond to the fundamental TE-like and the TM-like modes, respectively. As seen in Fig. 8, a disagreement in the modal reflectivity values of the fundamental TE-like mode is observed in general at relatively large values of Δx, as predicted by both the semivectorial and full-vectorial models for both situations. This discrepancy can be easily noticed when $\Delta x > 0.3\,\mu$m for the first situation ($L = 0\,\mu$m) and $\Delta x > 0.8\,\mu$m for the second situation ($L = 0.1\,\mu$m). On the other hand, the modal transmissivities as predicted by both the semivectorial and full-vectorial models are

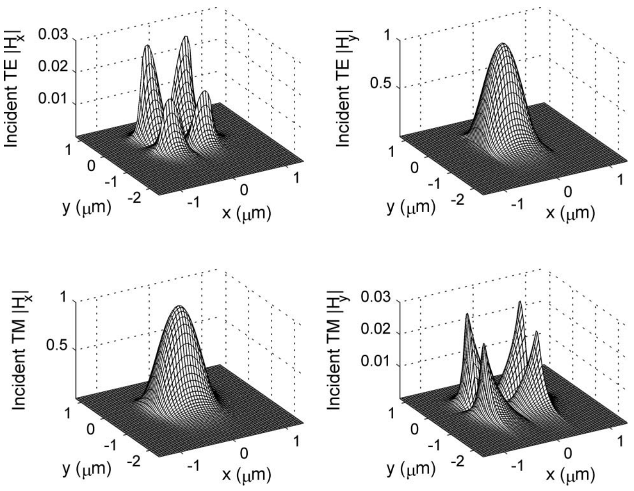

Fig. 5. Magnitude of the incident fundamental TE-like and TM-like modes corresponding to the coupled channel waveguides shown in Fig. 2(b) at the operating wavelength $\lambda = 1.55\,\mu$m and core width $w_x = 1\,\mu$m.

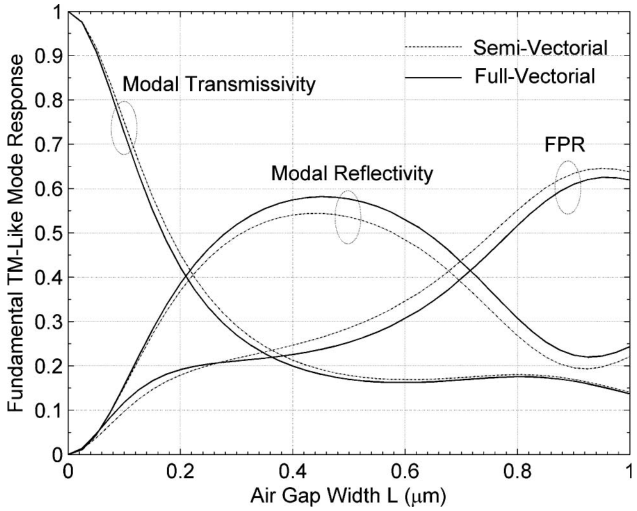

Fig. 7. Fundamental TM-like mode response corresponding to the coupled channel waveguides shown in Fig. 2(b).

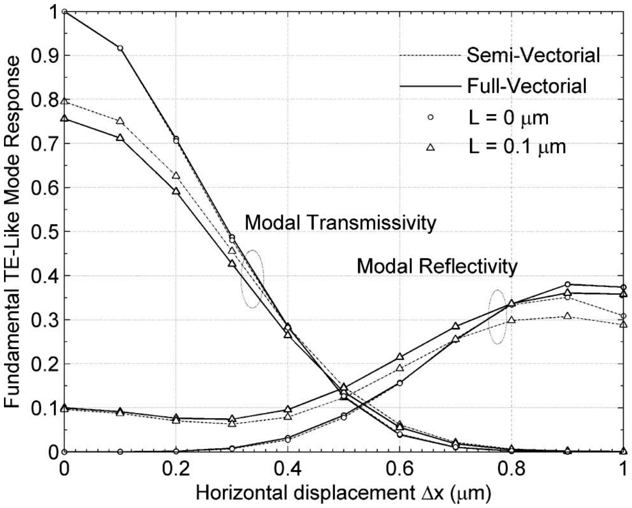

Fig. 8. Fundamental TE-like mode response corresponding to the coupled channel waveguides shown in Fig. 2(b) when the output (right) waveguide is displaced in the horizontal direction.

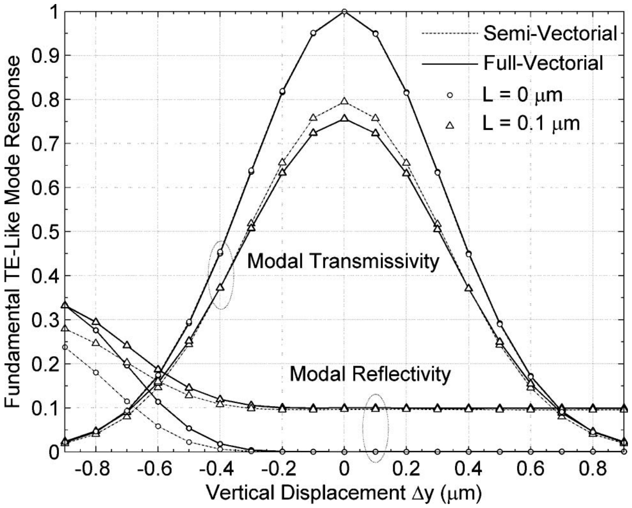

Fig. 10. Fundamental TE-like mode response corresponding to the coupled channel waveguides shown in Fig. 2(b) when the output (right) waveguide is displaced in the vertical direction.

generally in good agreement throughout the range of the horizontal displacement Δx for the case of directly coupled waveguides ($L = 0\,\mu$m). However, in the case of waveguide coupling through an air gap ($L = 0.1\,\mu$m), the modal transmissivity values calculated by the semivectorial and the full-vectorial model show some discrepancy when $\Delta x < 0.4\,\mu$m. The fundamental TM-like mode response of the structure (Fig. 9) again depicts similar behavior of the modal transmissivity and reflectivity curves as predicted by the semivectorial and full-vectorial models for both situations. In Figs. 8 and 9, the modal reflectivity tends to stabilize at a nonzero value when Δx exceeds a value of roughly $0.8\,\mu$m, while the modal transmissivity tends to zero in this same range. The reason for this behavior is obvious, since beyond this relatively large horizontal displacement, the output waveguide is effectively replaced by air, causing the stabilized nonzero modal reflectivity. The output waveguide also becomes sufficiently displaced away from the input modal field, resulting in negligible power coupling. Because the waveguide structure is symmetrical with respect to the vertical axis; the results associated with negative values of the horizontal displacement Δx are expected to be identical to these obtained using positive values of Δx.

Another possibility for transverse separation is when the horizontal axis of the output waveguide shown in Fig. 2(b) is displaced vertically with respect to the horizontal axis (x axis) of the input waveguide. This displacement is termed the vertical displacement Δy throughout this paper. The modal reflectivity and transmissivity variation with Δy are shown in Figs. 10 and 11, corresponding to the TE-like and the TM-like modes, respectively. Again, two situations ($L = 0\,\mu$m and $L = 0.1\,\mu$m) are considered here. In this case, the arrangement is asymmetric

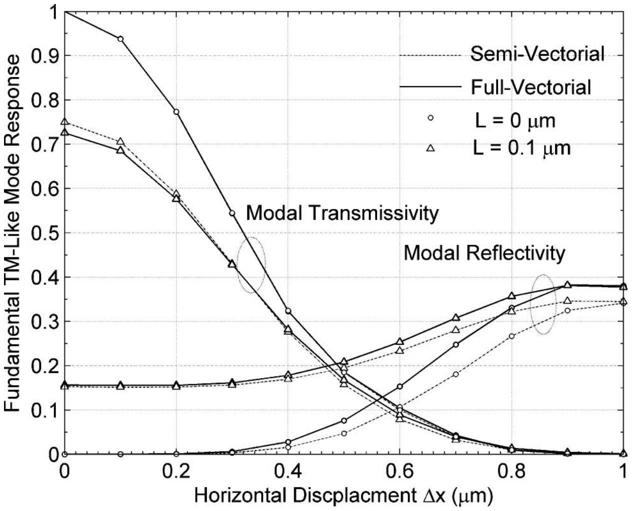

Fig. 9. Fundamental TM-like mode response corresponding to the coupled channel waveguides shown in Fig. 2(b) when the output (right) waveguide is displaced in the horizontal direction.

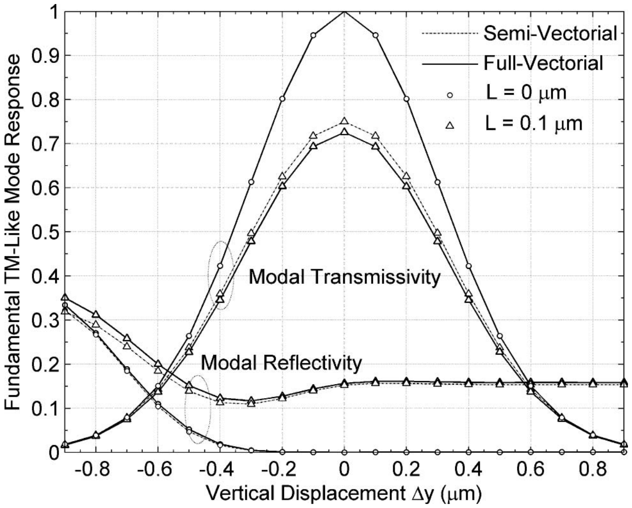

Fig. 11. Fundamental TM-like mode response corresponding to the coupled channel waveguides shown in Fig. 2(b) when the output (right) waveguide is displaced in the vertical direction.

with respect to horizontal axis; the results of both the negative and the positive vertical displacements are shown in Figs. 10 and 11. Both of these figures show a significant variation in the modal reflectivity and transmissivity values corresponding to $L = 0\,\mu\text{m}$ and $L = 0.1\,\mu\text{m}$, as predicted by both the semivectorial and full-vectorial models. In general, the modal reflectivity value is noticeably large when the vertical displacement Δy is negative (i.e., downwards displacement of the output waveguide). This is due to the input fundamental mode seeing air as the second region when Δy becomes more negative, whereas, for positive values of Δy, the modal reflectivity value reaches a steady-state value. For the situation where the waveguides are coupled by an air gap, the steady-state values of the fundamental TM-like and the TE-like mode reflectivities are, respectively, 0.15 and 0.1. The steady-state modal reflectivity value corresponding to the direct coupling of the two waveguides, for both the TE-like mode and the TM-like mode, is observed to be very low ($\approx 10^{-4}$). This is certainly due to the input mode's seeing the substrate of the output waveguide as the second region, which corresponds to a low-index-contrast longitudinal interface. In general, the modal transmissivity value corresponding to $L = 0\,\mu\text{m}$ is identical, as predicted by both the semivectorial and full-vectorial models, from Figs. 10 and 11. However, the modal transmissivity corresponding to the coupling of two waveguides with an air gap ($L = 0.1\,\mu\text{m}$) shows significant difference in the range $-0.2\,\mu\text{m} \le \Delta y \le 0.2\,\mu\text{m}$. The modal transmissivity values predicted by the full-vectorial model are observed to be somewhat lower than the prediction of the semivectorial model.

4. Conclusion

In this paper, two coupled raised channel waveguides that exhibit a high index contrast in both the longitudinal and transverse dimensions has been analyzed. The numerical results of both longitudinal and transverse misalignments showed a substantial difference in the power coupled to the output waveguide and the power reflected back into the input waveguide, as predicted by both the semivectorial and the full-vectorial models. The difference in the calculated results obtained by both models is observed to be somewhat larger for the TE-like case when compared to the TM-like case.

The authors gratefully acknowledge King Fahd University of Petroleum and Minerals, Dhahran, Saudi Arabia, for supporting this research work through research grant SB 070017.

References

1. H. B. Lin, Y. H. Wang, and W. S. Wang, "Single mode 1 × 3 integrated optical branching circuit design using micro prism," Electron. Lett. **30**, 408–409 (1994).
2. W. C. Chang and H. B. Lin, "A novel low-loss wide-angle Y-branch with a diamond-like micro prism," IEEE Photon. Technol. Lett. **11**, 683–685 (1999).
3. H. A. Jamid, Md. Zahed. M. Khan, and Md. Ameeruddin, "A compact 90° three branch beam splitter based on resonant coupling," J. Lightwave Technol. **23**, 3900–3906 (2005).
4. I. D. Villar, I. R. Matias, and F. J. Arregui, "Fiber-optic multiple-wavelength filter based on one dimensional photonic bandgap structures with defects," J. Lightwave Technol. **22**, 1615–1621 (2004).
5. A. M. Kenis, I. Vorobeichik, M. Orenstein, and N. Moiseyev, "Non-evanescent adiabatic directional coupler," IEEE J. Quantum Electron. **37**, 1321–1328 (2001).
6. C. Manolatou, M. J. Khan, S. Fan, P. R. Villeneuve, H. A. Haus, and J. D. Joannopoulos, "Coupling of modes analysis of resonant channel add–drop filters," IEEE J. Quantum Electron. **35**, 1322–1331 (1999).
7. Y. Chiou and H. Chang, "Analysis of optical waveguide discontinuities using the Padé approximants," IEEE Photon. Technol. Lett. **9**, 964–966 (1997).
8. L. A. Vielva, J. A. Pereda, A. Vegas, and A. Prieto, "Simulating 3D waveguide discontinuities using a combination of Prony's method and FDTD with improved absorbing boundary conditions," IEE Proc. Microwaves Antennas and Propag. **141**, 127–132 (1994).
9. T. Rozzi, L. Zappelli, and M. N. Husain, "Radiation modes and step discontinuities in dielectric rib waveguide," IEEE Trans. Microwave Theory Tech. **40**, 1879–1888 (1992).
10. G. Kweon, I. Park, and J. Shim, "A computational method of determining reflectance at abrupt waveguide interfaces," J. Lightwave Technol. **14**, 2436–2443 (1996).
11. N. N. Feng and W. P. Huang, "A Field-based numerical method for three-dimensional analysis of optical waveguide discontinuities," IEEE J. Quantum Electron. **39**, 1661–1665 (2003).
12. B. N. A. Rahman, J. B. Davies, "Analysis of optical waveguide discontinuities," J. Lightwave Technol. **6**, 52–57 (1988).
13. K. Kawano, T. Kitoh, M. Kohtoku, T. Takeshita, and Y. Hasumi, "3-D semivectorial analysis to calculate facet reflectivities of semiconductor optical waveguides based on the bi-directional method of line BPM (MoL-BPM)," IEEE Photon. Technol. Lett. **10**, 108–110 (1998).
14. M. Reed, P. Sewell, T. M. Benson, and P. C. Kendall, "Efficient propagation algorithm for 3D optical waveguides," IEE Proc. Optoelectron. **145**, 53–58 (1998).
15. K. Jiang and W. P. Huang, "A finite-difference-based mode matching method for 3-D waveguide structures under semivectorial approximation," J. Lightwave Technol. **23**, 4239–4248 (2005).
16. S. F. Helfert, A. Barcz, and R. Pregla, "Three-dimensional vectorial analysis of waveguide structures with the method-of-lines," Opt. Quantum Electron. **35**, 381–394 (2003).
17. H. A. Jamid and Md. Zahed. M. Khan, "3-D full-vectorial analysis of strong optical waveguide discontinuities using Padé approximants," IEEE J. Quantum Electron. **43**, 343–349 (2007).
18. H. A. Jamid and Md. Zahed M. Khan, "A numerical approach for full-vectorial analysis of 3-D guided wave structures with multiple and strong longitudinal discontinuities," IEEE J. Quantum Electron. **45**, 117–124 (2009).
19. S. H. Wei and Y. Y. Lu, "Application of bi-CGSTAB to waveguide discontinuity problems," IEEE Photon.Technol. Lett. **14**, 645–647 (2002).
20. H. A. Jamid, "Enhanced PML performance using higher order approximation," IEEE J. Microwave Theory Tech. **52**, 1166–1174 (2004).